Hard X-ray nano-holotomography with a Fresnel zone plate

SILJA FLENNER,[1] ADAM KUBEC,[2] CHRISTIAN DAVID,[2] MALTE STORM,[3] CLEMENS F. SCHABER,[4] FRITZ VOLLRATH,[5] MARTIN MÜLLER,[1] IMKE GREVING,[1,7] AND JOHANNES HAGEMANN[6,8]

[1]*Helmholtz-Zentrum Geesthacht, Max-Planck-Str. 1, 21502 Geesthacht, Germany*
[2]*Paul Scherrer Institut, Forschungsstr. 111, 5232 Villigen-PSI, Switzerland*
[3]*Diamond Light Source Ltd., Didcot, Oxfordshire OX11 0DE, UK*
[4]*Functional Morphology and Biomechanics, Zoological Institute, Kiel University, 24098 Kiel, Germany*
[5]*Department of Zoology, University of Oxford, Oxford, UK*
[6]*Deutsches Elektronen Synchrotron, Notkestr. 85, 22107 Hamburg, Germany*
[7]*imke.greving@hzg.de*
[8]*johannes.hagemann@desy.de*

Abstract: X-ray phase contrast nanotomography enables imaging of a wide range of samples with high spatial resolution in 3D. Near-field holography, as one of the major phase contrast techniques, is often implemented using X-ray optics such as Kirkpatrick-Baez mirrors, waveguides and compound refractive lenses. However, these optics are often tailor-made for a specific beamline and challenging to implement and align. Here, we present a near-field holography setup based on Fresnel zone plates which is fast and easy to align and provides a smooth illumination and flat field. The imaging quality of different types of Fresnel zone plates is compared in terms of the flat-field quality, the achievable resolution and exposure efficiency i.e. the photons arriving at the detector. Overall, this setup is capable of imaging different types of samples at high spatial resolution of below 100 nm in 3D with access to the quantitative phase information.

1. Introduction

X-ray nanotomography is a powerful tool to image objects in three dimensions (3D) with high spatial resolution in materials science, biology as well as in medicine. Especially for low absorbing samples, phase contrast methods such as propagation-based [1–4] and grating-based [5] phase contrast are frequently used. At the nano scale, there are two major full-field tomography techniques in use, namely Zernike phase contrast [6,7] and near-field propagation based microscopy in a cone beam setting (near-field holography, NFH) [8]. NFH at the nano scale is usually performed using Kirkpatrick-Baez (KB) mirrors, conceivably combined with X-ray waveguides [9,10]. This technique does allow for nanotomography at high temporal resolutions [11]. For Zernike phase contrast, most commonly Fresnel zone plates (FZP) and beamshaping condensers are used [12–15]. The condenser provides a high flux on the sample, but due to the FZP used as an objective lens behind the sample, the flux on the detector is significantly reduced. In contrast to NFH, full-field Zernike phase contrast does usually not allow to retrieve the phase signal quantitatively.

Fresnel zone plates [16] have widely been used as objective lenses in full-field and scanning transmission X-ray microscopes for many years. Being diffractive optics, their efficiency is mostly determined by the height of the structures. Especially for hard X-rays, the efficiency is usually in the range of <10%, limited by the achievable aspect ratio. Nevertheless, using an FZP as focusing optics, a small symmetric focus of down to 50 nm is commonly achievable.

Due to the lower structure height required for soft X-rays, a smaller focus of 12 nm is routinely reached [17]. Focal spot sizes of 7.8 nm have been reported also for hard X-rays, however at low efficiencies <1% [18]. Multilayer Laue lenses (MLL) in contrast are highly efficient and generate a comparably small focus [19,20]. These however need extensive alignment and create a large offset with respect to the optical axis, which is not feasible at all beamlines. In addition they usually have a very small aperture, which creates the need for pre-focusing. While other optics such as compound refractive lenses (CRL), KB-mirrors and especially waveguides also need precise and time consuming alignment, the proposed FZP based holography setup can be installed relatively fast and easy. Being a rotationally symmetrical 2D structure, usually no rotational alignment is needed for FZPs.

First attempts of using an FZP based holography setup have been made for soft X-rays in 2D [21]. However, using an FZP as a focusing element has one disadvantage: The zero diffraction order or primary beam is not focused by the FZP and thus must be blocked by a beamstop. Usually, a round, centered beamstop is used, resulting in a dark spot in the center of the image. Especially for tomography, this is a problem and leads to artifacts in the 3D reconstruction.

In this article, the concept of using an FZP based NFH setup for nanotomography in the hard X-ray regime is evaluated for the first time. Here, we used a tungsten wedge, covering one half of the FZP including the zero order, resulting in an off-axis geometry and circumventing the use of a centered beamstop.

## 2. Method and materials

2.1. Experimental setup

The off-axis hard X-ray NFH setup has been implemented at the imaging beamline P05 [13,22,23] (Fig. 1(a)) operated by Helmholtz-Zentrum Geesthacht at the PETRA III storage ring at DESY, Hamburg, Germany. The X-ray beam is monochromized using a Si-111 double crystal monochromator (DCM) to an energy of 11 keV with a $\Delta E/E$ of $1 \cdot 10^{-4}$. The experimental setup is shown in Fig. 1(b): The monochromatic beam is focused by an FZP. Several designs for the fabrication process of the FZP were considered, manufactured and tested (Table 1) to evaluate their aptitude for an NFH setup. The goal was to find the FZP design which gives the best compromise of a smooth illumination, focal spot size and usable flux on the detector.

Table 1. Different zone plates were tested to find the optimal illumination. The results are visialized in the corresponding panels of Fig. 2. The focus size was calculated from the aperture and focal length of the lenses, as described in section 3.1. The effective focus size accounts for the effect of the partial coherence by calculating the convolution of the geometrical image of the source and the theoretical focus size of the FZP.[a]

Type	Full FZP	Off-axis	Off-axis	Full FZP, stitched	Full FZP
Material	iridium	iridium	gold	gold	gold
Full diameter / μm	300	960	960	960	300
Outer most zone witdh d_r / nm	50	50	50	60	50
Focal lenght / mm	113.1	425.9	425.9	511	113.1
Theoretical focus size / nm	61	150*	150*	73	61
Geometrical image of source / nm	74	232	232	279	74
Effective focus size / nm	95	276	276	288	95
Panel Fig. 2	d	e	c	b	a

[a]The values marked with asterisk (*) are approximated due to the rectangular shape of the aperture.

Iridium based zone doubled structures have demonstrated superior properties in terms of achievable efficiency due to the high aspect ratio with a structure height of 400 nm. Iridium
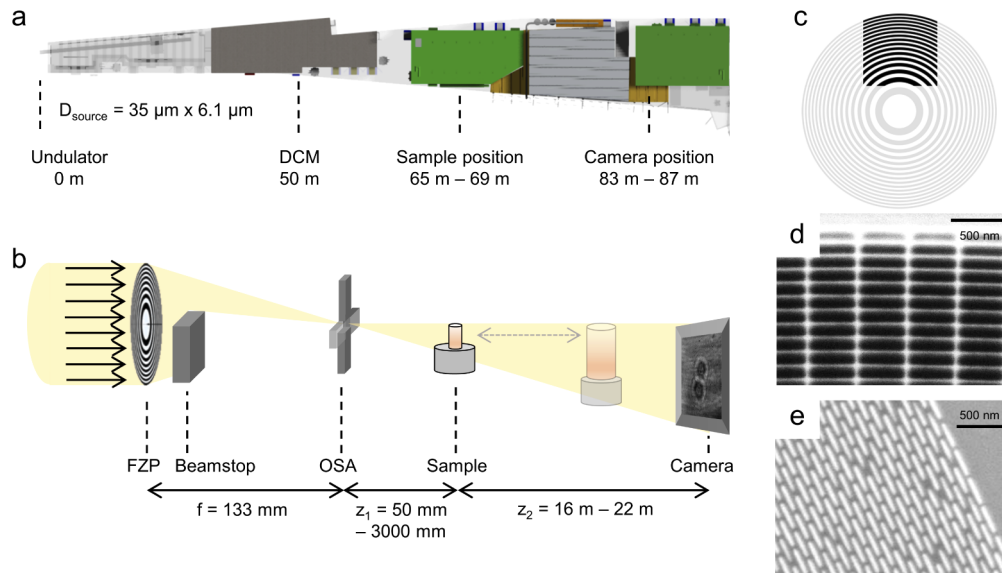
Fig. 1. (a) Beamline overview with relevant hardware components and their distances to the source. (b) NFH setup. The FZP focuses the coherent part of the beam to a small focal spot. The beamstop blocks the zero order. The OSAs block the higher diffraction orders from the FZP. The sample can be placed at different defocus positions in the divergent beam. After a propagation distance of approximately 16 m, the camera records the holographic projection of the sample. (c) Layout of an off-axis FZP. (d),(e) Different FZP designs. (d) The HSQ template used for the iridium FZPs with its support structures before the ALD processing step. The support structures are arranged perpendicular to the fields. (e) The structure of the gold FZP is arranged brick-like.

FZPs are manufactured with a template made of hydrogen silsesquioxane (HSQ); subsequently the actual zone structure is deposited by atomic layer deposition (ALD) on top of the existing structure [24]. For FZPs with a high aspect ratio it is necessary to incorporate support structures preventing the structures from collapsing (Fig. 1(d)). A completely different design is chosen for gold FZPs. The manufacturing process is explained in detail in [25]. For the design of the gold FZPs we used a brick like geometry (Fig. 1(e)) circumventing the use of continuous support structures perpendicular to the zone structures.

In order to separate zero and diffracted orders, the center part of the FZP needs to be blocked by a beamstop (Fig. 1(b)). Since this would conventionally result in a dark center area in the final image, half of the FZP is covered by a beamstop. As a consequence, the area of the FZP's used ("effective aperture") and thus the total flux on the sample is reduced by half. Therefore, an FZP with a large diameter is chosen to achieve a larger aperture. The diameter of the used FZP is however limited by the capabilities of the e-beam writer which is currently limited to a field size of 320 μm at the required resolution. Larger structures can be manufactured but will have imperfections in the stitching regions and may have reduced optical properties. Another approach to increase the effective aperture is to manufacture only the necessary part of the FZP resulting in an off-axis zone plate (Fig. 1(c)). Currently, one major application for off-axis zone plates is spectroscopy with resonant inelastic X-ray scattering (RIXS) [26]. Modified off-axis zone plates have also been employed as beam splitters at X-ray free electron lasers [27].

The presented tomographic measurements were performed using a gold FZP with a diameter of 300 μm and an outer-most zone width of $d_r = 50$ nm. In order to block the unfocused beam, a beamstop (scatter-less tungsten, 2 mm thickness) is placed in close proximity behind the FZP.

The order sorting apertures (OSA) are placed in the focal distance $f = 133$ mm and block the higher orders from the zone plate. The sample is mounted on a high precision rotation stage and can be moved along the optical axis on an air-bearing slider to a defocus distance of up to 5 m. The detector is placed in the adjacent experimental hutch at a sample to detector distance z_2 of up to 22 m (Fig. 1(a)). With the chosen optics the detector is already fully illuminated at a distance of 16 m. Due to this large sample to detector distance available at the instrument, no light optical magnification is needed. This is an advantage, since typical detector systems [28] used for this purpose consist of a scintillator paired with a microscope objective to decrease the effective pixel size of an optical camera, suffer from a low quantum efficiency. An X-ray sCMOS camera (Hamamatsu C12849-101U, $P_{det} = 6.5$ µm pixel size, 2048×2048 pixel, 16 bit image depth) with a 10 µm Gadox scintillator was used as a detector. The scintillation layer is directly coupled to the sCMOS chip resulting in a high photon efficiency. In between the sample and the camera, vacuum pipes are installed to reduce air scattering and absorption. Depending on the sample size, the desired field of view and resolution, the sample is placed in the diverging beam. The exit wavefield of the sample propagates through free-space which is described by the Fresnel propagator [29]. The intensities of the resulting near-field diffraction pattern the so-called in-line hologram are recorded by the detector. The magnification $M = (z_1 + z_2)/z_1$ and the effective pixel size $P_{eff} = P_{det}/M$ can be changed by moving the sample to a different defocus distance z_1. Usually, one distance is sufficient to perform a reconstruction for homogeneous, low absorbing specimens justifying the assumption of a pure phase object. In most cases, however, measurements at several defocus distances are needed in order to retrieve the phase quantitatively. In this case, a displacement of 1 mm between the defocus distances is found to induce sufficient variation in the holograms for the phase reconstruction.

2.2. Samples

Two different sample systems have been imaged to show the versatile application of the presented NFH setup. As a first sample system, low absorbing spider attachment hairs were used. Located at the spiders' feet, these 5 µm to 10 µm thick and up to 1 mm long hairs enable these animals to stick to surfaces and even walk upside down [30–33]. The attachment system is build up hierarchically. A single attachment hair is comprised of smaller hairs (microtrichia) with diameters of 150 nm to 300 nm and flattened adhesive tip structures. The principle of these hairs could be used to develop dry sticky adhesives. For the data presented in this study, one unstained and one stained hair of the wandering spider *Cupiennius salei* were used. The latter was stained with iodine and phosphor-tungstic acid. The single attachment hairs were glued on top of conical sample holders.

As a second sample system, elephant ivory was studied. In contrast to the spider attachment hairs, this material is not a pure phase object. Due to its outstanding material properties, ivory recently received an increasing interest [34–36]. The samples were obtained from seizures by the UK HM Revenue and Customs. A cylindrical sample of 20 µm diameter taken from the outer part of the tusk was mounted on a sample holder using focused ion beam (FIB) milling. This leads to a deposition of highly absorbing gallium on the sample. Therefore, the phase retrieval of this sample is demanding and not possible using direct inversion reconstruction approaches like the contrast transfer function (CTF). However, NFH allows imaging and reconstruction of multi-material samples with high density differences.

2.3. Data processing

To obtain the 3D reconstructions from the raw data recorded at one to three defocus distances, several data processing steps are necessary. First, the raw holographic projections are flat-field corrected. Due to temporal fluctuations in the illumination caused e.g. by the top-up refilling of PETRA III or mechanical instabilities of the monochromator, a simple flat-field correction is not sufficient. Thus, the fluctuations have to be taken into account. A series of flat-field images was

acquired before and during the acquisiton of the tomographic projections, to sample different states of the illumination. For each recorded holographic projection image, the best-fitting flat field was then calculated from the principal components of this series [37,38].

In the second step, the holograms recorded at different defocus distances were aligned and rescaled according to the computed magnifications (Fresnel scaling [39]) in order to enable phase reconstructions. The variation in propagation distance adds further information, which are needed for the subsequent phase retrieval step.

The third step, the phase reconstruction, was computed with up to three holograms using an iterative projection algorithm [38,40]. The iterates x_n of the algorithm are given by $x_{n+1} = P_S(P_M(x_n))$, i.e. alternating projections (AP). The projector P_M computes the projection based on the measured intensities. In case of multiple defocus distances, this is applied in an averaged manner as described in Hagemann et al. [40].

The sample plane constraints P_S should be chosen to match the properties of the sample under reconstruction. In the case of both sample types, a support and a value range constraint were applied. The support has been found automatically based on thresholding and morphological operations during the run of the reconstruction. In the range constraint, the allowed values of the reconstruction were limited to resemble a pure-phase object by setting the transmitted amplitude to 1 and restrict phases only to negative values in the case of the spider hair. For the ivory, it was necessary to allow for variations also in the absorption.

After the phase reconstruction, the reconstructed projections were aligned using the Scale-Invariant Feature Transform (SIFT) [41] provided as ImageJ plugin. The tomographic reconstructions were performed with the gridrec algorithm [42] and a Shepp-Logan filter using TomoPy [43].

The 3D resolution was estimated via the Fourier Shell Correlation (FSC) [44]. The projections were divided in two stacks and reconstructed separately. The reconstructed stacks were then used as the input for the FSC and the $1/2$ - bit threshold criterion was applied to calculate the resolution.

3. Results

3.1. Comparison of different FZPs

Various parameters are responsible for the final image resolution and quality (i.e. absence of artifacts). Artifacts arise mainly by imperfections of the flat-field correction. Therefore, a smooth illumination is preferable, since it can be corrected with less artifacts [45]. The resolution is limited by the focal spot size of the focusing optics, but is also influenced by the degree of coherence [46] and chromaticity [47] of the illumination. In general, the resolution is limited by $d_{res} = k \cdot \frac{\lambda}{2NA}$. In case of a circular FZPs, this depends on the outer most zone width ($d_{res} = 1.22 \cdot d_r$). In case of off-axis FZPs, the missing angles and the shape of the aperture have to be considered i.e. $d_{res} \approx k \cdot \frac{2r_o}{r_o - r_i} d_r$, where r_o and r_i are the inner and outer radius of the off-axis FZP. For a rectangular shape, k is approximately 1 [48,49]. Taking this into account, we calculated the approximated focus size in Table 1.

An important aspect effecting the resolution of a large FZP are the coherence properties of the source. Calculating the transversal coherence length of the undulator source of the beamline P05 reveals that the coherently illuminated area is limited, especially in horizontal direction: The transversal coherence length as calculated by $L_T = (\lambda R)/(2D)$ at a distance $R = 65$ m from the source (size $D = 35$ µm in horizontal and $D = 6.1$ µm in vertical direction) is 105 µm in horizontal direction and 600 µm in vertical direction. Ideally, the aperture of the FZP is chosen to be in the range of the transversal coherence length. A larger aperture can cause a loss of resolution, since the FZP is not coherently illuminated and the focus size increases. To account for the effect of partial coherence, the size of the spot delivered by the zone-plate objective has to

be described by a convolution of the geometric image of the source and the point spread function of the optics [50].

However, in perspective of the highly increased coherent flux available at 4th generation sources [51], different types of FZP designs (Table 1) were tested as focusing optics to evaluate their aptitude for the presented NFH setup regarding photon flux on the detector and flat-field quality.

First, iridium FZPs were used for focusing the beam. By using iridium for manufacturing the FZPs, it is possible to obtain larger aspect ratios, especially with outermost zone widths significantly below 50 nm. In addition to a full 300 μm FZP, an iridium off-axis FZP was tested. Due to the larger aperture of the off-axis FZP, five times more counts are recorded at the detector. Iridium FZPs require a certain type of support structures which generate a spoke-like structure in the flat-field, see Fig. 1(d). These spokes are a high spatial frequency artifact, which does not correct well [45], making them unsuitable for near-field holography.

For small outermost zone widths, FZPs made from gold usually have a lower efficiency due to the smaller aspect ratio achievable. In the cone beam geometry however, these optics produce a significantly smoother flat-field (Fig. 2(a-c)), resulting in a flat-field corrected hologram with less artifacts. The reason for this is to be found in the difference in design namely the absence of support structures. There are significantly more counts on the detector when using the gold instead of the iridium optics: The 300 μm gold FZP yields about 1.5 times and the off-axis gold FZP yields 1.7 times more counts than the corresponding iridium optics.

Using a 320 μm × 320 μm off-axis FZP part of a 960 μm FZP (Fig. 1(d)) yields higher flux, but less fringes are visible (Fig. 2(c,e)). Due to the off-axis geometry, the expected focus size of the off-axis FZPs increases to approximately 150 nm. Since the aperture of the off-axis zone plate is about three times larger than the horizontal coherence length, the FZP cannot be fully coherently illuminated, most likely causing an additional loss of resolution. Taking into account the partial incoherenct illumination, the focus increases to 276 nm (Table 1). This is already at the limit of resolving the finest structures of the spider attachment hair. Additional challenges and limitations for off-axis focusing optics might arise e.g. due to higher chromaticity requirements and possibly smaller required zone widths (as discussed in [52] for MLLs). In this case, the resolution is not sufficient to resolve the microtrichia on the spider hair. Therefore, despite their high flux, off-axis zone plates cannot be used for high resolution NFH.

Using a full FZP with 960 μm diameter with outer-most zone width of 60 nm yields a theoretical focus size of d_{res} = 73.2 nm. This FZP however, did not show more visible fringes, indicating a low resolution. The aperture of the FZP is much larger than the coherence length in horizontal but also in vertical direction. Thus the theoretical focus size is not reached, limiting the achievable resolution in NFH. Additionally, imperfections of the stitching process during manufacturing can also contribute to an enlargement of the focus for example through overlapping illumination speckles. Remember, each of these speckles is created by one of the e-beam fields.

The gold FZP with 300 μm diameter gave the best results in terms of flat-field quality and resolution and was therefore used for the following tomographic acquisitions. Using this FZP, the measured flux at the detector is 1.5×10^9 photons /s and comparable to a combination of KB mirror and waveguide used in [9].

3.2. Evaluation of test specimen

For the tomographic scans, 900 projections with an exposure time of 1 s were recorded. Depending on the composition of the sample, one to three distances are needed for the phase reconstruction. One distance takes approximately 30 min to acquire, including time for motor movement and camera readout. The total exposure time for one distance is 900 s, i.e. 15 min and therefore comparable to a classical transmission X-ray microscope (TXM) tomography scan [53].
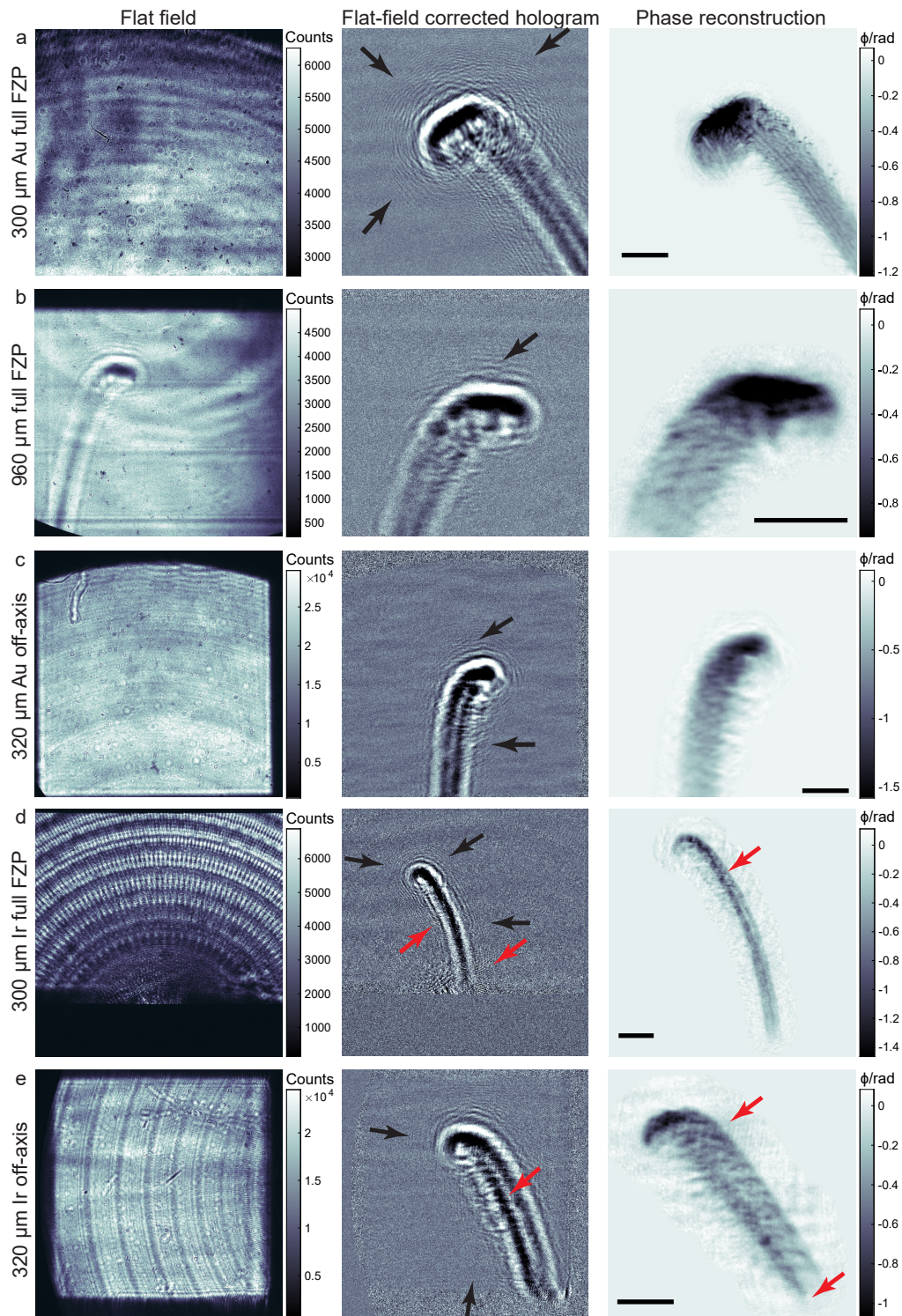
Fig. 2. Comparison of the performance of different FZPs. Left column: Uncorrected flat field. Middle column: Flat-field corrected hologram of the sample. Right column: Phase reconstruction of the sample. Scale bar: 10 μm. Black arrows point on smallest fringes visible. a) "Gold standard" 300 μm diameter gives a homogenous flat field. Spots originate from inclusions in the diamond beam exit window. A large number of fringes is visible in the flat field corrected hologram. Many details are visible in the reconstructions. b, c, e) In the corrected holograms of the 960 μm diameter Au FZP, off-axis Au FZP, and off-axis Ir FZP, only few fringes are visible. The corresponding reconstructions suffer therefore from low resolution. d, e) Iridium FZPs: support structures generate a structured flat field which causes artefacts in the flat-field corrected projections and in the reconstructions (red arrows).

In order to achieve a reasonable signal on the detector in TXM, a condenser optics with a large aperture in the mm-range is used to illuminate the sample creating a high flux in the sample plane [53]. A large fraction of this flux is however not transmitted to the detector due to the low efficiency of the objective zone plate. In contrast to TXM, NFH is a lensless imaging technique, so no flux is lost due to inefficient optics placed behind the sample. Thus, the dose is much lower in NFH compared to standard TXM.

The stained spider hair was measured at a defocus distance of 65 mm resulting in a magnification of 250× and an effective pixel size of 26 nm. The holograms and reconstruction of the spider attachment hairs is displayed in Fig. 3. In the flat-field corrected hologram of the stained hair, fringes are visible in both vertical and horizontal direction over the whole image as indicated by the arrows in Fig. 3(a). The phase reconstruction (Fig. 3(b)) of this sample was done using three distances. The structure of the hair can clearly be visualized and single microtrichia are well resolved. Spherical structures at the end of the hairs originate from the staining and cover the fine attachment platelets. The staining is therefore leading to severe changes in the structure.
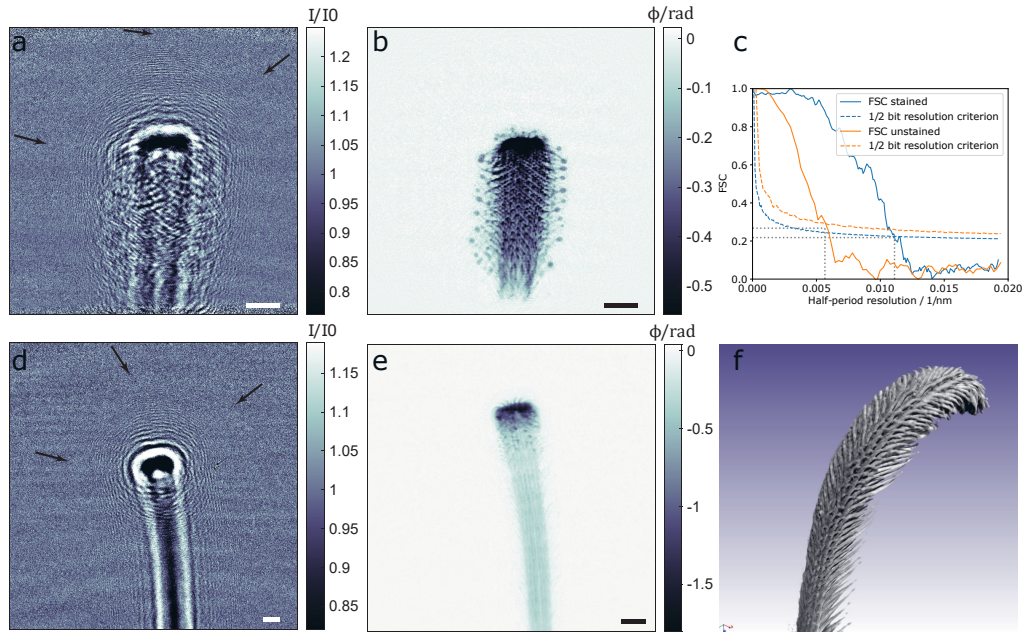
Fig. 3. Holotomography of a spider hair. (a) Flat-field corrected hologram of a stained spider hair at 250× magnification. Finest fringes are indicated by arrows. (b) Phase reconstruction of (a) using three distances. (c) Resolution determined by Fourier shell correlation of the 3D reconstructed spider hair. The best determined resolution is 90 nm at a pixel size of 26 nm. (d) Flat field corrected projection of an unstained spider hair at lower magnification (127×). (e) Phase reconstruction of (d) using 2 distances. (f) 3D rendering of the unstained spider hair. Scale bars: 5 µm

The unstained spider hair was measured at a defocus distance of 166 mm resulting in a magnification of 125× and an effective pixel size of 52 nm. Compared to the stained spider hair, reduced contrast is observed (Fig. 3(d)). This is supposedly due to the staining with heavier elements. Nevertheless, the phase can be easily reconstructed using two distances, as shown in Fig. 3(e,f).

Both sample preparations, stained and unstained, can be reconstructed at high quality, resolving the finest structures of the hair in 3D without artefacts. Although the unstained hair has less contrast in the hologram, a direct comparison is difficult due to the different magnifications used.

Because of the staining induced artefacts at the ends of the small hairs, the use of unstained samples is preferable. The quality of the reconstructions is comparable, meaning the smallest features can be resolved and the signal-to-noise ratio is sufficient to easily segment the spider hair using a simple threshold segmentation (Fig. 3(f)). This shows the high phase sensitivity of NFH for biological specimen, which allows imaging without staining.

As calculated from the FSC, a half-period resolution of 90 nm was achieved in 3D at a pixel size of 26 nm for the stained spider hair (Fig. 3(c)). This is well above of the theoretical Rayleigh resolution ($= 1.22 \cdot d_r = 61$ nm) and corresponds to 3.5 pixel of the detector, close to the detectors point spread function of 3 pixels, meaning that the resolution is predominately limited by the detector system. Other factors like the partial coherence or the sample movement occurring during the tomographic scans can also reduce the resolution. Due to the larger pixelsize of 52 nm, the determined resolution for the unstained sample was much lower (176 nm). The achieved spatial resolution in 3D is comparable to the resolutions recently reached by transmission X-ray microscopy at the same instrument (absorption 64 nm, Zernike phase contrast 81.9 nm) [53].

The ivory holograms were recorded at a magnification of $127\times$ i.e. at an effective pixel size of 51 nm (Fig. 4(a)). Due to the gallium coating and therefore strong absorption on the rim of the
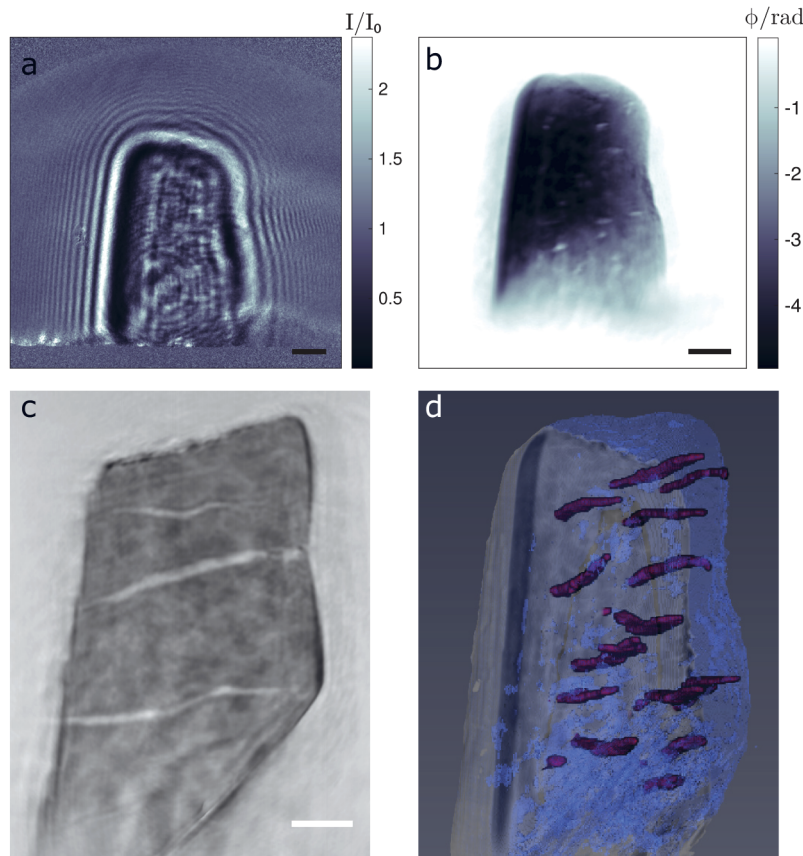
Fig. 4. Holotomography of ivory. (a) Flat-field corrected projection. (b) Phase reconstruction of (a) using three distances showing the projected phases. The gallium crust is located in the right. (c) Tomographic reconstruction, slice in xz direction. (d) 3D rendering of the tomographic reconstruction with segmented channels (magenta) inside the ivory and Ga crust on the left. Scale bars: 5 μm

sample, the phase reconstruction was computed from three distances and needed more complex processing. Figure 4(b) shows the phase reconstruction of a projection showing some tubules inside the ivory as well as the gallium crust on the right. In the tomographic reconstruction, the tubules, as well as density variations in the ivory matrix (flaky like structure) can be visualized. Not only the low absorbing ivory itself, but also the high absorbing gallium crust could be reconstructed without artifacts (Fig. 4(c,d)).

4. Conclusion and outlook

In this paper, we showed that with off-axis illumination for near-field holography using a simple FZP it is possible to obtain high quality 3D reconstructions of different sample types. The advantages of the NFH configuration of the P05 nanotomography endstation are an easy straight forward setup and high flexibility due to large range of possible propagation distances. The fine structures of the spider hair as a pure phase object, as well as the multi-material ivory sample including highly absorbing parts can be visualized. For the implementation of a FZP based NFH setup, the choice of a suitable FZP design is crucial. FZPs fabricated from gold give the smoothest flat field while the support structures needed for the fabrication of iridium FZPs cause a strongly structured flat field. Due to the limited coherence of the beam, large aperture off-axis FZPs cannot be fully utilized for performing high resolution NFH currently. These could however be used for NFH with lower resolution but higher flux. Since the FZP aperture should match the coherence length of the beam, an FZP with a diameter of 300 µm is a good compromise between efficiency and achievable resolution. The advantages of the setup using the full 300 µm gold FZP are the clear and smooth flat field allowing for artefact free reconstruction and its simplicity and therefore fast setup installation time. A waveguide-based setup yields both a comparable flat field and similar flux density [9], but requires a more complex alignment procedure, not suitable for a versatile beamline where different techniques are offered and fast setup switching is beneficial.

A new channelcut monochromator has been installed at the beamline, providing a much more stable illumination. This is supposed to create an easier flat field correction leading to less artifacts in the reconstructions.

This setup could greatly benefit from a 4th generation source [51]. The higher and isotropic coherence allows the use of even larger zone plates. The improved beam parameters and higher coherent flux will lead to a reduction in scan time, making this setup suitable for *in situ* experiments.

Disclosures

The authors declare no conflicts of interest.

References

1. A. Snigirev, I. Snigireva, V. Kohn, S. Kuznetsov, and I. Schelokov, "On the possibilities of x-ray phase contrast microimaging by coherent high-energy synchrotron radiation," Rev. Sci. Instrum. **66**(12), 5486–5492 (1995).

2. S. Mayo, T. Davis, T. Gureyev, P. Miller, D. Paganin, A. Pogany, A. Stevenson, and S. Wilkins, "X-ray phase-contrast microscopy and microtomography," Opt. Express **11**(19), 2289–2302 (2003).

3. M. Töpperwien, M. Krenkel, D. Vincenz, F. Stöber, A. M. Oelschlegel, J. Goldschmidt, and T. Saldilt, "Three-dimensional mouse brain cytoarchitecture revealed by laboratory-based x-ray phase-contrast tomography," Sci. Rep. **7**(1), 42847 (2017).

4. M. Krenkel, M. Töpperwien, C. Dullin, F. Alves, and T. Saldilt, "Propagation-based phase-contrast tomography for high-resolution lung imaging with laboratory sources," AIP Adv. **6**(3), 035007 (2016).

5. F. Pfeiffer, M. Bech, O. Bunk, P. Kraft, E. F. Eikenberry, C. Brönnimann, C. Grünzweig, and C. David, "Hard-X-ray dark-field imaging using a grating interferometer," Nat. Mater. **7**(2), 134–137 (2008).

6. F. Zernike, "Phase contrast, a new method for the microscopic observation of transparent objects," Physica **9**(7), 686–698 (1942).

7. G. Schmahl, D. Rudolph, G. Schneider, P. Guttmann, and B. Niemann, "Phase contrast x-ray microscopy studies," Optik **97**, 181–182 (1994).

8. P. Cloetens, W. Ludwig, J. Baruchel, D. Van Dyck, J. Van Landuyt, J. P. Guigay, and M. Schlenker, "Holotomography: Quantitative phase tomography with micrometer resolution using hard synchrotron radiation x rays," Appl. Phys. Lett. **75**(19), 2912–2914 (1999).

9. T. Saldilt, M. Osterhoff, M. Krenkel, R. N. Wilke, M. Priebe, M. Bartels, S. Kalbfleisch, and M. Sprung, "Compound focusing mirror and X-ray waveguide optics for coherent imaging and nano-diffraction," J. Synchrotron Radiat. **22**(4), 867–878 (2015).

10. R. Mokso, P. Cloetens, E. Maire, W. Ludwig, and J. Y. Buffire, "Nanoscale zoom tomography with hard x rays using Kirkpatrick-Baez optics," Appl. Phys. Lett. **90**(14), 144104 (2007).

11. J. Villanova, R. Daudin, P. Lhuissier, D. Jauffrès, S. Lou, C. L. Martin, S. Labouré, R. Tucoulou, G. Martínez-Criado, and L. Salvo, "Fast in situ 3D nanoimaging: a new tool for dynamic characterization in materials science," Mater. Today **20**(7), 354–359 (2017).

12. I. Vartiainen, M. Warmer, D. Goeries, E. Herker, R. Reimer, C. David, and A. Meents, "Towards tender X-rays with Zernike phase-contrast imaging of biological samples at 50 nm resolution," J. Synchrotron Radiat. **21**(4), 790–794 (2014).

13. I. Greving, S. Flenner, E. Larsson, M. Storm, F. Wilde, E. Lilleodden, T. Dose, H. Burmester, L. Lottermoser, C. David, and F. Beckmann, "Full-field hard X-Ray microscope designed for materials science applications," Microsc. Microanal. **24**(S2), 228–229 (2018).

14. M. Storm, F. Döring, S. Marathe, C. David, and C. Rau, "The diamond i13 full-field transmission x-ray microscope: a zernike phase-contrast setup for material sciences," *Powder Diffr.* 1–7 (2020).

15. B. Deng, Y. Ren, Y. Wang, G. Du, H. Xie, and T. Xiao, "Full-field x-ray nano-imaging at SSRF," X-Ray Nanoimaging: Instruments and Methods **8851**, 88511D (2013).

16. J. Kirz, "Phase zone plates for x rays and the extreme uv," J. Opt. Soc. Am. **64**(3), 301–309 (1974).

17. W. Chao, J. Kim, S. Rekawa, P. Fischer, and E. H. Anderson, "Demonstration of 12 nm resolution Fresnel zone plate lens based soft X-ray microscopy," Opt. Express **17**(20), 17669 (2009).

18. I. Mohacsi, I. Vartiainen, B. Rösner, M. Guizar-Sicairos, V. A. Guzenko, I. McNulty, R. Winarski, M. V. Holt, and C. David, "Interlaced zone plate optics for hard X-ray imaging in the 10 nm range," Sci. Rep. **7**(1), 43624 (2017).

19. W. Xu, W. Xu, N. Bouet, J. Zhou, H. Yan, X. Huang, A. Pattammattel, Y. Gao, M. Lu, M. Zalalutdinov, Y. S. Chu, and E. Nazaretski, "2D MEMS-based multilayer Laue lens nanofocusing optics for high-resolution hard x-ray microscopy," Opt. Express **28**(12), 17660 (2020).

20. A. Kubec, K. Melzer, J. Gluch, S. Niese, S. Braun, J. Patommel, M. Burghammer, and A. Leson, "Point focusing with flat and wedged crossed multilayer Laue lenses," J. Synchrotron Radiat. **24**(2), 413–421 (2017).

21. R. Heine, T. Gorniak, T. Nisius, C. Christophis, M. E. Pettitt, F. Staier, T. Wilhein, S. Rehbein, M. Grunze, and A. Rosenhahn, "Digital in-line X-ray holography with zone plates," Ultramicroscopy **111**(8), 1131–1136 (2011).

22. M. Ogurreck, F. Wilde, J. Herzen, F. Beckmann, V. Nazmov, J. Mohr, A. Haibel, M. Müller, and A. Schreyer, "The nanotomography endstation at the PETRA III Imaging Beamline," J. Phys.: Conf. Ser. **425**(18), 182002 (2013).

23. S. Flenner, E. Larsson, K. Furlan, D. Laipple, M. Storm, F. Wilde, R. Blick, G. A. Schneider, R. Zierold, R. Janssen, C. David, F. Beckmann, M. Muller, and I. Greving, "Nanotomography of Inverse Photonic Crystals Using Zernike Phase Contrast," Microsc. Microanal. **24**(S2), 148–149 (2018).

24. B. Rösner, F. Koch, F. Döring, J. Bosgra, V. A. Guzenko, E. Kirk, M. Meyer, J. L. Ornelas, R. H. Fink, S. Stanescu, S. Swaraj, R. Belkhou, B. Watts, J. Raabe, and C. David, "Exploiting atomic layer deposition for fabricating sub-10 nm X-ray lenses," Microelectron. Eng. **191**, 91–96 (2018).

25. S. Gorelick, J. Vila-Comamala, V. A. Guzenko, R. Barrett, M. Salomé, and C. David, "High-efficiency fresnel zone plates for hard X-rays by 100 keV e-beam lithography and electroplating," J. Synchrotron Radiat. **18**(3), 442–446 (2011).

26. F. Marschall, Z. Yin, J. Rehanek, M. Beye, F. Döring, K. Kubiček, D. Raiser, S. T. Veedu, J. Buck, A. Rothkirch, B. Rösner, V. A. Guzenko, J. Viefhaus, C. David, and S. Techert, "Transmission zone plates as analyzers for efficient parallel 2D RIXS-mapping," Sci. Rep. **7**(1), 8849 (2017).

27. F. Döring, B. Rösner, M. Langer, A. Kubec, A. Kleibert, J. Raabe, C. Vaz, M. Lebugle, and C. David, "Multi-focus off-axis zone plates for X-ray free-electron laser experiments," Optica **7**(8), 1007 (2020).

28. P. A. Douissard, A. Cecilia, X. Rochet, X. Chapel, T. Martin, T. van de Kamp, L. Helfen, T. Baumbach, L. Luquot, X. Xiao, J. Meinhardt, and A. Rack, "A versatile indirect detector design for hard x-ray microimaging," J. Instrum. **7**(09), P09016 (2012).

29. J. Goodman, *Introduction to Fourier Optics* (MaGraw-Hill, 1996), 2nd ed.

30. D. T. Roscoe and G. Walker, "The adhesion of spiders to smooth surfaces," Bull. Br. arachnol. Soc **8**, 224–226 (1991).

31. S. Niederegger and S. N. Gorb, "Friction and adhesion in the tarsal and metatarsal scopulae of spiders," J. Comp. Physiol., A **192**(11), 1223–1232 (2006).

32. C. F. Schaber, S. Flenner, A. Glisovic, I. Krasnov, M. Rosenthal, H. Stieglitz, C. Krywka, M. Burghammer, M. Müller, and S. N. Gorb, "Hierarchical architecture of spider attachment setae reconstructed from scanning nanofocus X-ray diffraction data," J. R. Soc. Interface. **16**(150), 20180692 (2019).

33. S. Flenner, C. F. Schaber, I. Krasnov, H. Stieglitz, M. Rosenthal, M. Burghammer, S. N. Gorb, and M. Müller, "Multiple mechanical gradients are responsible for the strong adhesion of spider attachment hair," Adv. Mater. **32**(37), 2002758 (2020).

34. F. Vollrath, R. Mi, and D. U. Shah, "Ivory as an important model bio-composite," Curator: The Mus. J. **61**(1), 95–110 (2018).

35. X. Lu, M. P. Fernández, R. S. Bradley, S. D. Rawson, M. O'Brien, B. Hornberger, M. Leibowitz, G. Tozzi, and P. J. Withers, "Anisotropic crack propagation and deformation in dentin observed by four-dimensional X-ray nano-computed tomography," Acta Biomater. **96**, 400–411 (2019).

36. M. Albéric, M. N. Dean, A. Gourrier, W. Wagermaier, J. W. Dunlop, A. Staude, P. Fratzl, and I. Reiche, "Relation between the macroscopic pattern of elephant ivory and its three-dimensional micro-tubular network," PLoS One **12**(1), e0166671 (2017).

37. V. V. Nieuwenhove, J. D. Beenhouwer, F. D. Carlo, L. Mancini, F. Marone, and J. Sijbers, "Dynamic intensity normalization using eigen flat fields in x-ray imaging," Opt. Express **23**(21), 27975 (2015).

38. J. Hagemann, M. Vassholz, H. Hoeppe, M. Osterhoff, J. M. Rosselló, R. Mettin, F. Seiboth, A. S. Johannes, Möller, J. Hallmann, C. Kim, M. Scholz, U. Boesenberg, R. Schaffer, A. Zozulya, W. Lu, R. Shayduk, A. Madsen, C. G. Schroer, and T. Salditt, "Single-pulse phase-contrast imaging at free-electron lasers in the hard X-ray regime," (in review).

39. D. Paganin, *Coherent X-Ray Optics* (Oxford University Press, 2006).

40. J. Hagemann, M. Töpperwien, and T. Salditt, "Phase retrieval for near-field X-ray imaging beyond linearisation or compact support," Appl. Phys. Lett. **113**(4), 041109 (2018).

41. D. G. Lowe, "Distinctive image features from scale-invariant keypoints," Int. J. Comput. Vis. **60**(2), 91–110 (2004).

42. B. A. Dowd, G. H. Campbell, R. B. Marr, V. V. Nagarkar, S. V. Tipnis, L. Axe, and D. P. Siddons, "Developments in synchrotron x-ray computed microtomography at the National Synchrotron Light Source," Dev. X-Ray Tomogr. II **3772**, 224–236 (1999).

43. D. Gürsoy, F. De Carlo, X. Xiao, and C. Jacobsen, "TomoPy: A framework for the analysis of synchrotron tomographic data," J. Synchrotron Radiat. **21**(5), 1188–1193 (2014).

44. M. Van Heel and M. Schatz, "Fourier shell correlation threshold criteria," J. Struct. Biol. **151**(3), 250–262 (2005).

45. C. Homann, T. Hohage, J. Hagemann, A.-L. Robisch, and T. Salditt, "Validity of the empty-beam correction in near-field imaging," Phys. Rev. A **91**(1), 013821 (2015).

46. J. Hagemann and T. Salditt, "Coherence-resolution relationship in holographic and coherent diffractive imaging," Opt. Express **26**(1), 242–253 (2018).

47. J. Hagemann, "X-ray near-field holography: Beyond idealized assumptions of the probe," Ph.D. thesis, Georg-August-Universität Göttingen (2017).

48. M. Born, E. Wolf, A. B. Bhatia, P. C. Clemmow, D. Gabor, A. R. Stokes, A. M. Taylor, P. A. Wayman, and W. L. Wilcock, *Principles of Optics: Electromagnetic Theory of Propagation, Interference and Diffraction of Light* (Cambridge University Press, 1999), 7th ed.

49. D. Attwood, *Soft X-Rays and Extreme Ultraviolet Radiation: Principles and Applications* (Cambridge University Press, 1999).

50. C. Jacobsen, S. Williams, E. Anderson, M. T. Browne, C. J. Buckley, D. Kern, J. Kirz, M. Rivers, and X. Zhang, "Diffraction-limited imaging in a scanning transmission x-ray microscope," Opt. Commun. **86**(3-4), 351–364 (1991).

51. C. G. Schroer, I. Agapov, W. Brefeld, R. Brinkmann, Y.-C. Chae, H.-C. Chao, M. Eriksson, J. Keil, X. N. Gavaldà, R. Röhlsberger, O. H. Seeck, M. Sprung, M. Tischer, R. Wanzenberg, and E. Weckert, "PETRA IV: the ultralow-emittance source project at DESY," J. Synchrotron Radiat. **25**(5), 1277–1290 (2018).

52. H. Yan and Y. S. Chu, "Optimization of multilayer Laue lenses for a scanning X-ray microscope," J. Synchrotron Radiat. **20**(1), 89–97 (2013).

53. S. Flenner, M. Storm, A. Kubec, E. Longo, F. Doring, D. M. Pelt, C. David, M. Muller, and I. Greving, "Pushing the temporal resolution in absorption and Zernike phase contrast nanotomography: Enabling fast in situ experiments," J. Synchrotron Radiat. **27**(5), 1339–1346 (2020).